



**Environmental
Science**
Nano

**Emerging investigator series: Kinetics of Diopside Reactivity
for Carbon Mineralization in Mafic-Ultramafic Rocks**

Journal:	<i>Environmental Science: Nano</i>
Manuscript ID	EN-ART-02-2023-000087.R1
Article Type:	Paper

SCHOLARONE™
Manuscripts

Paper

Emerging investigator series: Kinetics of Diopside Reactivity for Carbon Mineralization in Mafic-Ultramafic Rocks[†]

Received 00th January 2023,
Accepted 00th February 20xx

DOI: 10.1039/x0xx00000x

Briana Aguila,^{a*} Landon Hardee,^a H. Todd Schaefer,^b Siavash Zare,^c Mohammad Javad Abdolhosseini Qomi,^c Jarrod V. Crum,^b Jade E. Holliman Jr.,^d Elena Tajuelo Rodriguez,^e Lawrence M. Anovitz,^f Kevin M. Rosso,^d Quin R. S. Miller^{b*}

The ongoing use of fossil fuels to supply modern energy demands has necessitated research on combating carbon dioxide (CO₂) emissions and climate change. Carbon storage via mineral trapping in basalt and related rocks is a promising strategy. However, mineralization rates depend on the variable mineralogy that makes up these rock formations. Diopside (CaMgSi₂O₆) is a common pyroxene mineral in ultramafic and mafic rocks including basalt, but relatively little work has been done to understand its carbon mineralization kinetics using hydrated supercritical CO₂, which induces the formation of reactive nanoscale interfacial water films. *In situ* XRD experiments at 50–110°C and 90 bar indicate that diopside transforms into a myriad of Mg/Ca carbonates, including huntite [Mg₃Ca(CO₃)₄] and very high magnesium calcite (VHMC, *i.e.*, protodolomite). Through *ex situ* characterization, we were able to constrain reaction pathways for the dissolution-precipitation transformation process including metastable intermediate precipitates. Experiments performed at variable temperatures enabled Avrami-derived rate constants and an apparent activation energy of 97 ± 16 kJ/mol, implying the dissolution of diopside is the rate-limiting step. Density functional theory (DFT) calculations, used to gain molecular insight into the surface stability of the diopside during dissolution, suggest that exposed calcium cations are susceptible to dissolution when put in contact with water given their coordination environment. The collective results point to the high CO₂ mineralization potential of diopside in basalts, which could help guide parameterization of reactive transport models

Emerging investigator series:

To combat increasing carbon dioxide (CO₂) emissions a permanent storage solution is required, with carbon mineralization at the forefront of research. To implement this strategy work must be done to understand the nanoscale reaction pathways and stability of the resulting carbonate products. Diopside is a silicate mineral that is highly prevalent in basalt formations, however, its complex multi-ion composition leads to a variety of possible carbonate products. This study used a suite of experiments to analyse the carbonation pathways and kinetics of diopside at temperatures and pressure relevant to CO₂ storage. Our results provide a better understanding of diopside carbonation and are key steps towards large-scale carbon storage to offset CO₂ emissions and create more sustainable industries.

needed to design and permit commercial-scale subsurface carbon storage operations.

Introduction

Since the onset of the industrial revolution carbon dioxide (CO₂) emissions have increased, with exponential growth in the past 75 years. An estimated 36.3 gigatonnes was released in 2021

due to anthropogenic sources and the numbers are only expected to climb without any mitigation measures.¹ It is well known that this increase in CO₂ and other gases has enhanced the global greenhouse effect and is the main culprit of climate change and ocean acidification. If allowed to continue the Earth's temperature will keep rising which will have detrimental effects to the environment, aquatic life, and overall human health.

Although the renewable energy sector is growing, it is not enough to meet global energy needs and thus coal power will still be required in the immediate future. One approach to mitigate CO₂ emissions is to utilize carbon capture and sequestration (CCS) processes.² This approach takes inspiration from the natural carbon cycle, wherein subsurface rocks store CO₂ from the atmosphere as stable carbonate minerals. However, it would take thousands of years to passively convert

^a Department of Chemistry, Francis Marion University, Florence, SC 29506, USA
Email: briana.aguila@fmarion.edu

^b Energy and Environment Directorate, Pacific Northwest National Laboratory, Richland, WA 99352, USA
Email: quin.miller@pnnl.gov

^c Department of Civil and Environmental Engineering, Henry Samueli School of Engineering, E4130 Engineering Gateway, University of California, Irvine, Irvine, CA 92697, USA

^d Physical and Computational Sciences Directorate, Pacific Northwest National Laboratory, Richland, WA 99352, USA

^e Nuclear Energy and Fuel Cycle Division, Oak Ridge National Laboratory, Oak Ridge, TN 37830, USA

^f Chemical Sciences Division, Oak Ridge National Laboratory, Oak Ridge, TN 37830, USA

[†] Electronic Supplementary Information (ESI) available: Table S1–S2 and Figures S1–S7, supplemental *in situ* and *ex situ* XRD plots and TGA-MS data.
See DOI: 10.1039/x0xx00000x

all the CO₂ that is now present. To combat this issue, CO₂ can be injected into basaltic formations, which is known to be much more reactive than sedimentary rocks, as they contain metal cations, such as magnesium, calcium, and iron, which will readily form metal-carbonates.³⁻⁵ Originally, carbon dioxide removal (CDR) scenarios targeted capturing CO₂ from large point sources for subsequent transport and injection into the subsurface.⁶ More recently though, driven by private investment and tax incentives, modular direct air capture (DAC) systems⁷ have expanded siting options for future CO₂ storage projects.

While research continues on methods to capture CO₂, ongoing studies at the laboratory scale highlight the feasibility of basalt rock for converting CO₂ into stable carbonates. Field-scale tests at the Wallula Basalt Carbon Storage Pilot Project (SE Washington, USA) and CarbFix (SW Iceland) have demonstrated successful mineralization of supercritical CO₂ (scCO₂) and aqueous-dissolved CO₂, respectively.⁸⁻¹³ These complementary endeavors are demonstrating permanent carbon storage technologies that leverage rapid reactivity in mafic formations.^{14, 15} It is clear basalt can convert CO₂ into stable carbonate minerals, but more work is needed to address multiscale knowledge gaps related to mineralization outcomes and timescales that are required for designing and implementing commercial-scale storage.

Forsteritic olivine (nominally Mg₂SiO₄) has received by far (c.f. ^{14, 16-18}) the most attention of any mineral for carbon storage reactivity, due to its rapid carbonation kinetics^{17, 19-25}, structural and chemical simplicity, along with its prevalence in ultramafic rocks and many basalt formations. In contrast, relatively little mineral carbonation research has been conducted on more abundant and widespread minerals that have more complex structures and compositions. The pyroxene group is another type of mineral class that is commonly found in basalt and other mafic-ultramafic rock formations.²⁶ The pyroxene group has the general formula XYZ₂O₆ and is characterized as an inosilicate. Within this class, diopside (CaMgSi₂O₆) is of great interest due to its natural reactivity,^{27, 28} abundance, and complex multi-ion composition, which provides a multitude of possible carbonate products once exposed to injected CO₂. Extensive work²⁹⁻⁴⁹ has been focused on pyroxene dissolution kinetics and mechanisms and also on pyroxene carbonation.^{26, 50-56} However, there is a dearth of reported results^{54, 55, 57, 58} for the carbonation of diopside or its reactivity in wet scCO₂ fluids, which are vital to understand the fate and transport of anthropogenic subsurface CO₂ in mafic and ultramafic rocks.

This present investigation focuses on the kinetics and pathways of diopside mineralization at relevant temperatures and pressure to simulate downhole conditions (>850 m) of subsurface carbon storage reservoirs, including Pacific Northwest National Laboratory's Wallula site.^{8, 59} The experimental conditions focused on the reactivity of diopside in water-poor scCO₂-dominant environments, where the carbon mineralization transformation occurs in reactive nanoscale

interfacial water films and water behaves as a catalyst.¹⁴ Through a combination of *in situ* high pressure X-ray diffraction (XRD) and a suite of *ex situ* sample characterization we were able to identify the carbonate products as well as the transient and amorphous phases that formed during diopside carbonation experiments. A kinetic analysis of the carbonation at variable temperatures allowed us to calculate the energy barrier required for diopside carbonation, which is the first reported kinetic data for carbon mineralization of diopside. This data was then supplemented by computational work to calculate the surface stabilities and the relative surface changes during dissolution. Overall, the goal of this work is to provide fundamental insight into carbon mineralization potential for a widespread and highly relevant mineral, helping secure a sustainable energy future.

Materials and Methods

Materials

The diopside used in this study was synthesized as previously reported.⁶⁰ The starting sample had a high specific surface area of 63.5 m²/g and was comprised of nanoparticles with a diameter of 50-100 nm. The phase purity and crystallinity were confirmed with XRD analysis (**Figure S1**) by comparing to the diopside powder diffraction file (PDF #019-0239) from the International Centre for Diffraction Data (ICDD).

In situ X-ray diffraction

Time-resolved *in situ* XRD experiments were conducted at 90 bar and 50-110 °C in a high-pressure static reactor with a beryllium cap and stainless-steel base. The *in situ* XRD experimental apparatus and procedures have been previously described in detail.⁶¹⁻⁶⁵ For all experiments, 30 μL of water was placed in the reactor reservoir to ensure that the scCO₂ was fully saturated. The diopside powder was lightly packed into the vertically oriented XRD sample holder not in contact with the water reservoir below. The reactor was preheated and stabilized at the desired temperature before pressurizing with 90 bar CO₂.

The *in situ* XRD reactor was housed in a Bruker D8 Discover Super Speed powder diffractometer equipped with an XYZΩ Materials Research Instruments TCP Temperature Chamber stage, horizontal goniometer, and a VANTEC-500 detector set at a 20 cm sample-to-detector distance. A 0.5 mm point source with a Montel mirror was operated at 50kV and 24mA power settings. The sample stage was positioned at 10°Ω and the detector was fixed at 28.5 °2θ, providing a °2θ range of 12-44°. The diffractometer automatically scanned the sample for 200-500 seconds (**Table 1**) with a nine second delay in between each pattern. The images were processed with Bruker AXS GADDS software and then imported into JADE XRD software to obtain peak positions, intensities, and phase identification through comparison with ICDD PDF database entries.

Ex situ sample characterization

All reacted samples were analysed with *ex situ* XRD to resolve reflections not visible *in situ*. The sample apparatus was first

Table 1. Experimental conditions and results for diopside carbonation experiments conducted at 50-110 °C and 90 bar scCO₂.*

Experiment ^a	Temperature (°C) ^b	Reaction Time (hr)	In situ XRD Scan Time (s)	Carbonate Mineral Assemblage ^c	Reaction Extent (%) ^d	Avrami k (s ⁻¹) ^e
I	110	136.3	200	huntite, ACC, aragonite	77	3.51E-03
II		20.7	200	huntite, ACC, aragonite	61	
III		3.9	300	huntite, ACC, aragonite	24	
IV	90	89.0	200	huntite, ACC, aragonite, magnesite	66	2.66E-04
V		44.2	200	huntite, ACC, aragonite	62	
VI		5.9	200	huntite, VHMC, ACC	18	
VII	50	166.5	200;500 ^f	aragonite, VHMC, AMC	38	9.70E-06
VIII		70.2	500	aragonite, VHMC, AMC	15	
IX		20.3	500	VHMC, APMC	8	

*Abbreviations: scCO₂ – supercritical CO₂; k- carbonation rate constant; ACC- amorphous calcium carbonate; VHMC- very high magnesium calcite with equal Mg and Ca; AMC- amorphous magnesium carbonate; APMC- amorphous calcium magnesium carbonate; XRD- high pressure X-ray diffraction; TGA-MS- thermogravimetric mass spectrometry; SEM-EDS- scanning electron microscopy energy dispersive spectroscopy.

^a Experiments were conducted at 90 bar with 30 μl of H₂O. Carbon dioxide density at 90 bar and 110, 90, and 50 °C is 154.93, 175.34, and 285 kg/m³, respectively.⁶⁶

^b H₂O solubility in 90 bar scCO₂ (mol %) is 2.509, 1.359, and 0.354 for 110 °C, 90 °C, and 50 °C, respectively. Calculated using solubility model of Spycher and Pruess.⁶⁷

^c Carbonate phases identified or inferred based on combination of XRD, TGA-MS, SEM-EDS, and mass balance; see Results and Discussion section.

^d Reaction extent for diopside carbonation based on TGA-MS results. Reaction extent of 100% defined as all Mg and Ca from diopside is incorporated into carbonate minerals. This reaction extent concept and calculation was used for our previous forsterite studies.^{21, 65, 68}

^e 10X the uncertainty calculated in SigmaPlot 12.5⁶⁹; Avrami R² of kinetic model fit for 110, 90, and 50 °C were 0.92, 0.96, and 0.95, respectively.

^f Scan time was changed to 500 s after 72 hr.

cooled to room temperature and depressurized, followed by removal of the beryllium cap. The reacted samples remained in the sample holder and patterns were collected from 12-64 °2θ.

Portions of the reacted samples were collected for thermogravimetric analysis coupled with mass spectrometry (TGA-MS) to calculate the reaction extent and confirm the carbonate species present. Briefly, 2-5 mg of sample was heated to 850 °C at a rate of 10 K/min with simultaneous monitoring of the ion currents for CO₂ (m/z=44) and H₂O (m/z=18). A temperature range of 35-850 °C was used for total mass loss determination. The reaction extent was calculated by comparing the experimental mass loss with the theoretical weight percent of carbonate products and their thermal decomposition reactions. The mass spectrometer tracked CO₂ and H₂O release to further confirm the types of carbonate species identified by XRD and inferred from mass balance.

Scanning electron microscopy coupled with energy dispersive spectroscopy (SEM-EDS) was used to determine the morphology and chemistry, respectively, of the products. Reacted samples were mounted on aluminum stubs using double sided carbon tape, sputter coated with 2nm of iridium, and analyzed with a JSM-7001F field-emission gun scanning electron microscope (SEM, JEOL USA, Inc. Peabody,

MA). Images were collected using a JEOL retractable low-working distance backscattered electron (BSE) detector. Energy-dispersive spectroscopy (EDS) was performed using a pair of opposing Bruker XFlash[®]6|60 (Bruker AXS Inc., Madison, WI) detectors to mitigate shadowing caused by sample typology. Data analysis was performed using Bruker ESPRIT (v2.0) software.

Carbonation kinetics calculations

Previously established kinetic models were applied to understand the rate of carbonate crystallization.^{17, 70} The reaction extents for each temperature, as shown in **Table 1**, were evaluated using the Avrami equation⁷¹ as expressed below:

$$\alpha(t) = 1 - e^{-kt^n} \quad (1)$$

where $\alpha(t)$ is the reaction extent as a function of time (t), n is an empirical constant, and k is the rate constant.⁷²⁻⁷⁶ This model is ideal for transformations with sigmoidal reaction profiles⁷⁷ and has been successfully applied to fluid-solid reactions⁷⁸ including carbonation.^{79, 80} The rate constants from the experiments were then used to calculate the apparent

ARTICLE

Environmental Science: Nano

activation energies (E_a) of diopside carbonation using the Arrhenius relationship given by:

$$k = A_a e^{\frac{-E_a}{RT}} \quad (2)$$

where R is the gas constant, T is the absolute temperature, and A_a designates a pre-exponential factor. The calculated E_a value is considered an apparent activation energy because of the complex dissolution-precipitation processes. Lines of best fit on the Arrhenius plot were determined via simple linear regression and the negative slopes divided by R resulted in the apparent activation energy of diopside carbonation in kJ/mol with a conservative uncertainty of ± 16 kJ/mol.

Density functional theory calculations

To calculate surface formation energies through Density Functional Theory (DFT), Vienna Ab-initio Simulation Package (VASP)⁸¹ was implemented. Projector augmented wave (PAW) potentials⁸² were used with the kinetic cut-off energy of 520 eV. The Perdew-Burke-Ernzerhof (PBE) generalized gradient approximation (GGA) was used as the exchange-correlation functional.⁸³ For the crystal surfaces, $2 \times 2 \times 1$ mesh points were used to sample the K-space using the Monkhorst-Pack scheme. The Conjugate gradient method was used for geometry optimization.

The (110) surface cleavage of the diopside was studied, which is the most observed surface. However, which metal sites are exposed at the surface has yet to be discovered. Therefore, the surface energies for four surface configurations were calculated. In each configuration, either calcium or magnesium was exposed at the surface. The surface formation energy was calculated through the following formula:

$$\gamma = \frac{E_{surf} - \frac{N_{surf}}{N_{bulk}} E_{bulk}}{2A} \quad (3)$$

where E_{surf} and E_{bulk} are the surface and bulk energies, respectively. N_{surf} and N_{bulk} are the number of atoms in surface and bulk configurations, respectively. A is the surface area. In each surface simulation case, the first two layers of the solid were free to move while the inner layers were kept fixed to represent the bulk phase.

Results and Discussion

Carbon mineralization pathways for diopside

Results from *in situ* and *ex situ* XRD experiments, TGA-MS, and SEM-EDS for **EXP I-IX** were used in concert to determine the effects of temperature (50-110 °C) on the carbonation pathways of diopside. These results, organized in **Table 1**, provide insight into the transient and amorphous phases that form on the path to long-term carbon dioxide sequestration in mafic and ultramafic rocks.

110 °C/90 bar. XRD waterfall plots (**Figure 1** and **Figure S2**) show rapid dissolution of diopside with precipitation of a crystalline carbonate phase identified as huntite⁸⁴⁻⁸⁹ [$Mg_3Ca(CO_3)_4$]. This was an unexpected result given the initial 1:1 Mg:Ca ratio of diopside transforming into a 3:1 ratio of the metal cations in huntite. Huntite has been implicated as an intermediate on the path to dolomite formation,^{85, 89, 90} sometimes appearing in Mg-Ca carbonate precipitation studies.⁹¹⁻⁹⁴ The *in situ* data provided no evidence of transient phases in **EXP I** and **EXP II** so **EXP III** was conducted to further resolve crystalline phases at the onset of precipitation. *Ex situ* XRD analyses was required to distinguish the aragonite ($CaCO_3$) phase present in **EXP III** indicating that huntite and aragonite begin to coprecipitate after 4 hours of

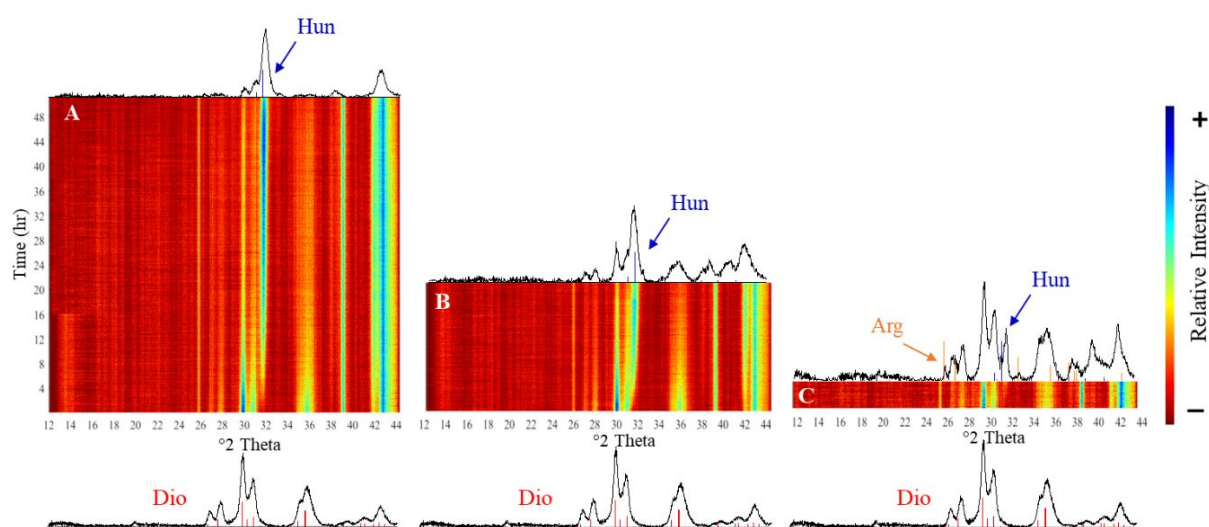


Figure 1. Carbonation of diopside as a function of time at 110 °C/90 bar supercritical CO_2 showing precipitation of huntite and aragonite. *In situ* XRD 2D waterfall plots with corresponding *ex situ* initial and final patterns for **EXP I** (A), **EXP II** (B), and **EXP III** (C).

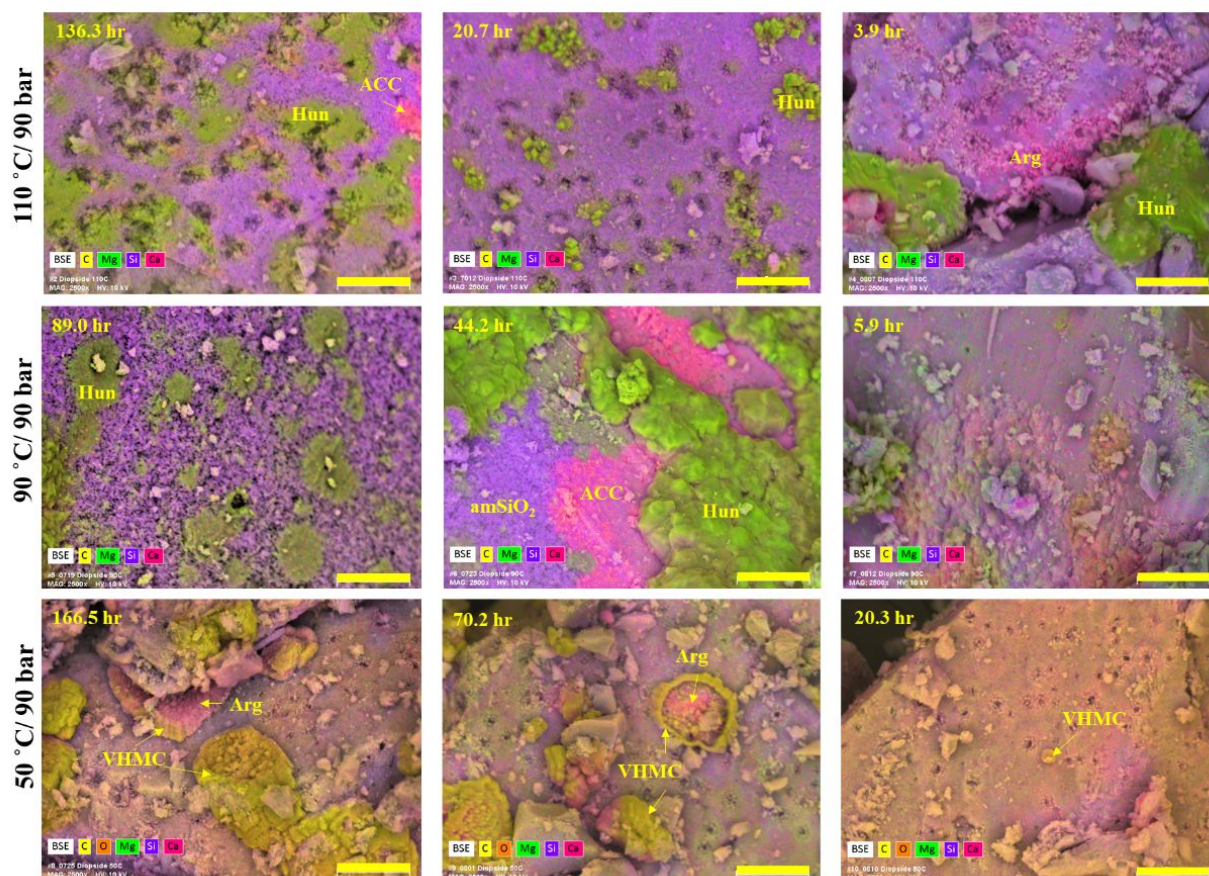


Figure 2. SEM-EDS composite images of samples from **EXP I-IX** post-reaction with mineral designation labels (**Table 1**). Colours correspond to elemental composition as indicated in the legend. Scale bars are 7 μm .

reaction time. Given the high magnesium content in the system, it is reasonable that aragonite is present over other polymorphs of CaCO_3 .⁹⁵ Aragonite, as opposed to calcite, precipitation in these experiments is likely due to the inhibitory effect of magnesium on calcite crystallization.^{96, 97} After closer examination of the **EXP I and II** *ex situ* XRD patterns small aragonite peaks are still present, providing further evidence of the coprecipitation of huntite and aragonite at 110 °C. As the reaction proceeds, the abundance of crystalline Ca-carbonate diminishes, creating a greater percentage of amorphous calcium carbonate (ACC) with increasing huntite formation.

TGA-MS was utilized on post-reacted samples to determine the carbonation reaction extent based on the carbonate species identified from XRD analyses (**Figure S3**). From the TGA, the total mass loss was determined for each sample and was used to calculate the reaction extent. From these results, we can see that the longer the reaction proceeds, the greater the reaction extent (**Table 1**), with **EXP I** having the largest value of 77%, followed by **EXP II** (61%) and **EXP III** (24%). The mass spectrometry results further validate the carbonate species identified. Huntite is expected to have two CO_2 peaks released associated with the decomposition reaction of 3 Mg: 1 Ca carbonate species,^{98, 99} as evidenced in the mass-normalized

mass spectrometry data (**Figure S4**) for **EXP I and II**. **EXP III**, with the more prevalent presence of aragonite with huntite has three CO_2 peaks as the sample decomposes.⁹⁹

SEM-EDS provides visual evidence of the phases identified by XRD and TGA-MS (**Figure 2**). **EXP I-III** images have regions of magnesium and carbon-rich areas attributed to huntite. Although huntite is present in all samples, the crystal size and definition vary as the reaction proceeds due to the continuous dissolution-precipitation during carbonation. **EXP I and III** images have calcium and carbon-rich areas indicating the presence of ACC and aragonite, respectively. This provides further evidence of ACC in **EXP I** given the substantial decrease in intensity of the aragonite peak on the *ex situ* XRD pattern.

90 °C/90 bar. **EXP IV-VI** XRD waterfall plots (**Figure 3** and **Figure S5**) have similar results to the experiments conducted at 110 °C with huntite formation beginning around 6 hours. There is evidence of small aragonite peaks for the **EXP IV and V** *ex situ* XRD patterns, suggesting the majority of calcium carbonate is amorphous. The *ex situ* scan of **EXP IV** also shows evidence of magnesite (MgCO_3) that is not present in **EXP V or VI**, highlighting the varied transient phases possible with a mixed metal system such as diopside. To better resolve the minute

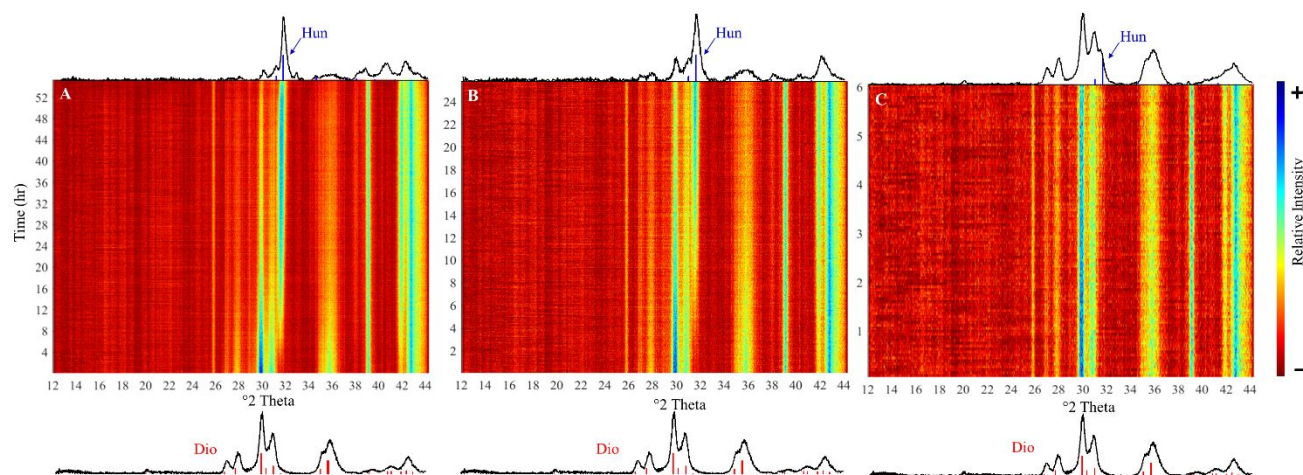


Figure 3. Carbonation of diopside as a function of time at 90 °C/90 bar supercritical CO₂ showing precipitation of huntite. *In situ* XRD 2D waterfall plots with corresponding *ex situ* initial and final patterns for **EXP IV (A)**, **EXP V (B)**, and **EXP VI (C)**.

changes in the XRD patterns for **EXP VI**, the initial and final patterns were normalized and overlaid (**Figure S6**). This allowed us to resolve a small shoulder representing the initial formation of huntite, as well as an increase in the peak intensity at 2.89 Å suggestive of very high magnesium calcite (VHMC) with nominally equal molar amounts of Ca and Mg, also known as disordered dolomite or protodolomite.¹⁰⁰⁻¹⁰² In this work, we follow the best practices nomenclature of Gregg et al.¹⁰¹ to not refer to these phases as a type of dolomite, as that implies cation ordering and so-called superstructure¹⁰³ (ordering) XRD reflections. The process of “huntinization”¹⁰⁴ is not well understood, especially in our context of Mg:Ca ratio for different phases changing from 1:1 (diopside) to 3:1 (huntite) to 1:1 (VHMC).

TGA-MS results for **EXP IV-VI** (**Figure S3** and **Figure S4**) follow suit with reaction extents having a rapid increase from 18% at 5.9 hours (**EXP VI**) to 62% within 44.2 hours (**EXP V**) and 66% as the reaction continues for 89.0 hours (**EXP IV**). The mass spectrometry results have two CO₂ peaks associated with huntite, containing successive decomposition of the two types of carbonates.⁹⁸ SEM-EDS imaging of **EXP IV** and **EXP V** samples delineated Ca-rich, Mg-dominant precipitates, consistent with huntite signatures observed with XRD and TGA-MS. The image collected for **EXP VI** was inconclusive with no identifiable regions of the carbonate products. The image for **EXP V** provided the best visual representation of the products with a silicon rich and magnesium/calcium poor area attributed to the amorphous silica by-product that is expected once the metal cations dissolve from the mineral and precipitate as carbonates. As well, there is a calcium and carbon rich area for the ACC that must be present to account for the mass-balance of calcium in the products.

50 °C/90 bar. XRD waterfall plots for **EXP VII-IX** were inconclusive due to the high CO₂ density at lower temperatures, wherein no peaks were able to be resolved *in situ* (**Figure S7**).

Analysis was then done solely based on *ex situ* patterns (**Figure 4**) with the appearance of aragonite for **EXP VII and VIII**, as well as evidence of VHMC with a steady increase in the peak intensity at 2.88 Å. To consider the Mg mass-balance there must also be amorphous magnesium carbonate (AMC) present as one of the products. A subtle hump in the XRD pattern prior to background subtraction further substantiates the presence of an amorphous phase, although that contribution may be partly a signal from amorphous silica. For **EXP IX** there is evidence of an increase in intensity for the peak positioned at 2.90 Å (**Figure**

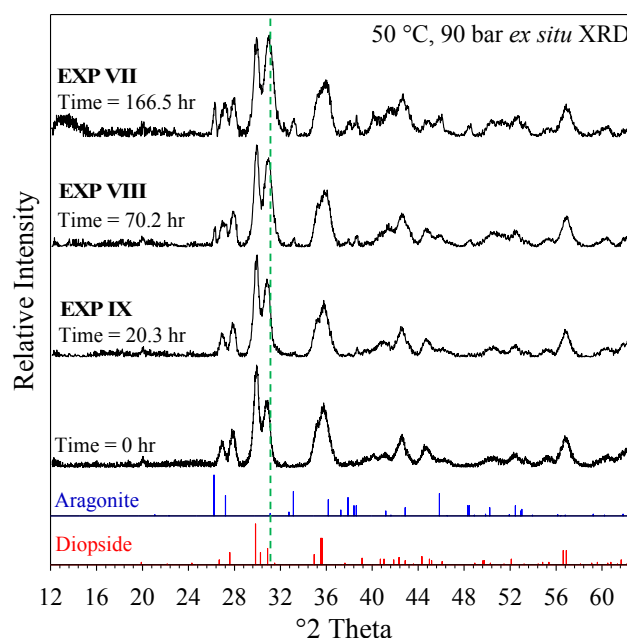


Figure 4. Depressurized post-reaction XRD patterns of diopside reacted with scCO₂ at 50 °C/90 bar. Green-dashed reference line is at d-spacing of 2.88 Å, suggestive of a VHMC phase (see text). *In situ* data sets are presented in **Fig. S7**.

S6) indicative of VHMC however, no further information can be gathered from XRD analysis.

TGA-MS results show low reaction extents only reaching 38% after 166.5 hours for **EXP VII**, which is rational given the lower temperature for this set of experiments (**Figure S3**). What is interesting is the mass spectrometry results, clearer in the mass-normalized MS overlay (**Figure S4**), with the early release of H₂O and CO₂ from 35-350 °C indicative of amorphous carbonate phases present in **EXP VII-IX**.^{63, 99, 105} Given that no other carbonates can be conclusively identified for **EXP IX**, based on the mass spectrometry data, we can infer that the early H₂O and CO₂ comes from the decomposition of an amorphous calcium magnesium carbonate (ACMC) with unknown proportions. We note that AMC and ACC may both incorporate Ca and Mg, respectively, leading to ACMC.¹⁰⁵⁻¹⁰⁸ The multiple CO₂ peaks for **EXP VII-IX** further confirm the variety of carbonates present in the samples post-reaction. SEM-EDS images for **EXP VII-IX** all have carbon rich regions with near equal amounts of calcium and magnesium indicating VHMC, which further supports the XRD results with an increase in peak intensity at 2.88-2.90 Å. The VHMC d₁₀₄ peak positions of 2.90-2.88 Å observed in this study correspond to compositions of ~45-52% MgCO₃.¹⁰⁹ **EXP VII and VIII** also show calcium and carbon rich areas attributed to aragonite.

A summary of carbonate mineral phase outcomes for diopside carbonation determined in this study is shown in **Figure 5**. The carbonate mineral assemblages identified through combined analyses from XRD, TGA-MS, SEM-EDS, and mass balance were graphed as a function of time for each temperature set in **Figure 6A**. This graph allows a better visual representation of the transient phases that form and offers insight into the complexities of the continued dissolution-precipitation of diopside carbonation. Since the diopside contains two distinct metal cations, there are a variety of metal carbonates in different ratios that can form. Initially, the magnesium and calcium begin to precipitate in near equal amounts as ACMC to VHMC.¹¹⁰ As dissolution continues at higher temperatures, the magnesium content increases due to the reduced solvation

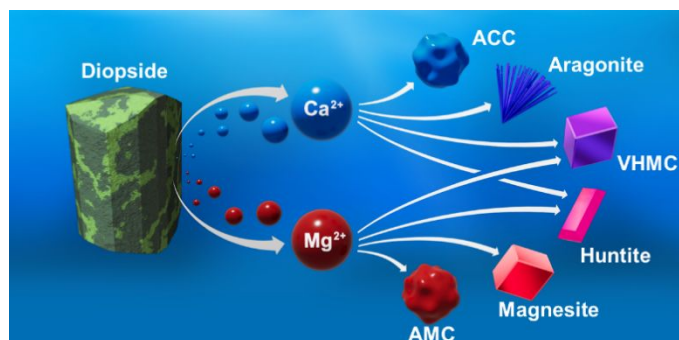


Figure 5. Conceptual graphic showing carbonate mineral phase outcome possibilities observed in the present study for calcium and magnesium cation released from dissolving diopside. The colour scheme consists of red Mg²⁺ and blue Ca²⁺, so the Mg:Ca ratio is reflected in the precipitate colour: red for 1:0 AMC and magnesite, magenta for 3:1 for huntite, purple for 1:1 VHMC, and blue for 0:1 ACC and aragonite.

energy barrier¹¹⁰ and begins forming huntite, while the remaining calcium precipitates as aragonite and ACC. If carbonation was allowed to continue, we propose that the calcium and magnesium ions would continue to order in a 1:1 ratio and form the thermodynamically stable product, dolomite [CaMg(CO₃)₂].^{104, 111} A preliminary *in situ* Raman spectroscopy reactivity study⁵⁷ of natural diopside in water-saturated scCO₂ (60°C and 79 bar, 0.49 mol% H₂O)⁶⁷ reported transitory huntite that increased in abundance before disappearing over the course of 49 days. That investigation highlighted the metastable nature of huntite during diopside carbonation, consistent with our reaction path interpretations. Longer-term studies, including *in situ* high-pressure infrared spectroscopy experiments are currently being conducted to better understand amorphous carbonate transformations and the possibility of achieving dolomite crystallization at relatively low temperatures.

Carbonation kinetics of diopside

The reaction extent results based on the TGA-MS data were plotted for each temperature vs time to better elucidate the kinetics of diopside carbonation. As shown in **Figure 6B**,

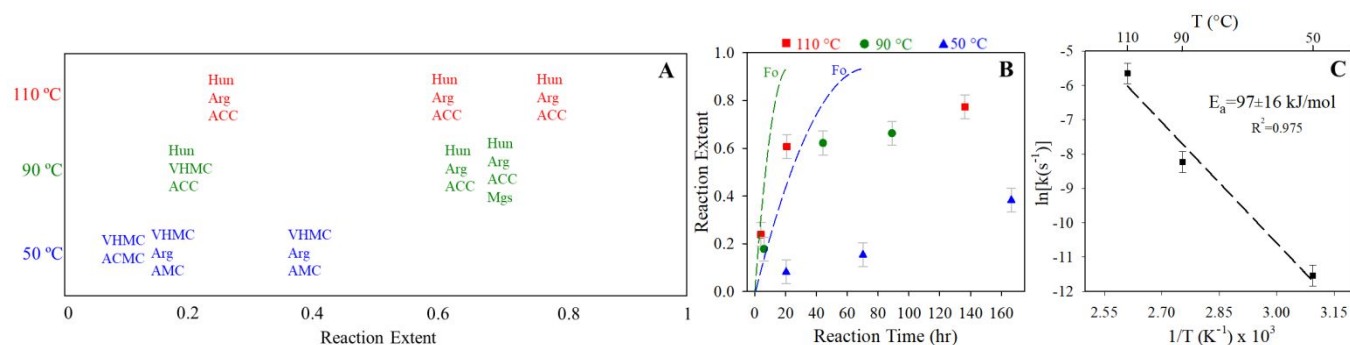


Figure 6. (A) Carbonate species identified through XRD analysis, TGA-MS, SEM-EDS, and mass balance for **EXP I-IX** versus their calculated reaction extent. (B) Time-dependent reaction extents for 50, 90, and 110 °C diopside carbonation experiments and (C) Arrhenius plot based on kinetic fit of rate constants derived from the Avrami equation. Diopside carbonation apparent activation energy is 97 ± 16 kJ/mol. The dashed curves comparative reaction extent trends determined in Miller et al.⁶⁵ for forsterite conversion to magnesite ($\text{Mg}_2\text{SiO}_4 + 2\text{CO}_2 = 2\text{MgCO}_3 + \text{SiO}_2$) at 50 °C (blue) and 90 °C (green).

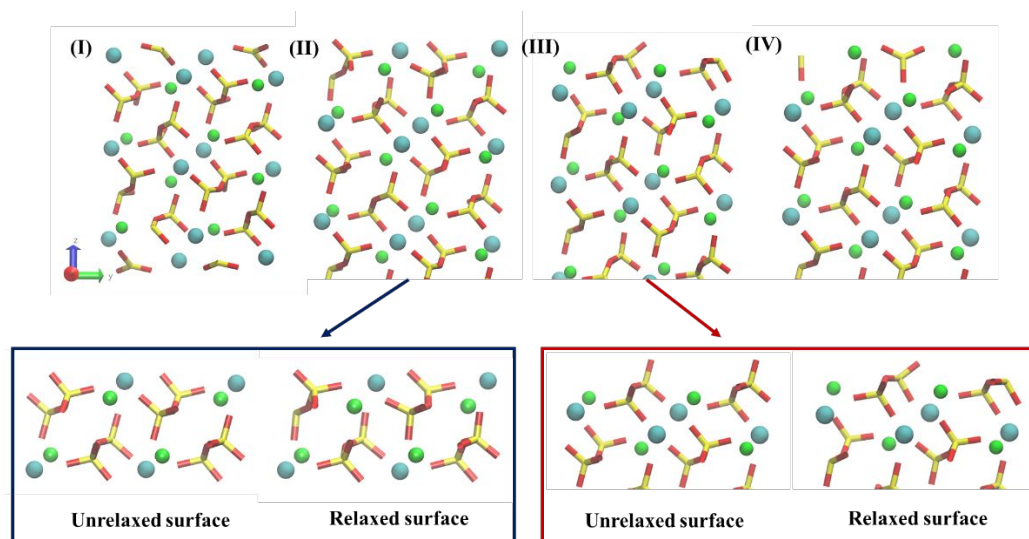


Figure 7. Atomistic representation of diopside (110) surfaces. Cases (I) to (IV) demonstrate a diopside (110) surface when the surface is cut at different locations along the z-axis. The relaxed surfaces in cases (II) and (III) show significant displacement between surface Ca (blue) and Mg (green) with respect to the second layer. Surface energies and coordination numbers are listed in Table S1 and Table S2, respectively.

forsterite carbonation determined in our previous study is substantially faster than that of diopside at the same experimental conditions of 50 or 90 °C and 90 bar in water-saturated sCO_2 . This disparity in reaction rates, even though the specific surface area of the diopside is ~ 2.4 times higher than that of the forsterite (63.5 vs. 26.7 m^2/g), is likely due to the slower dissolution rate of diopside relative to that of olivine.¹¹² This discrepancy in reaction (dissolution and/or carbonation) rates between olivine and pyroxenes is also documented for enstatite (MgSiO_3) and forsterite.^{39, 52, 113} The chain silicate diopside has polymerized silica requiring more bond breakages, as opposed to the isolated silica tetrahedra of orthosilicate forsterite. Additionally, based on the thermo.dat^{114, 115} thermodynamic base, the free energy change for forsterite conversion to magnesite is more negative than that of diopside dolomitization. We are continuing to explore these types of mineral structure-reactivity differences for pyroxene, olivine, and mafic glass, particularly in the context of interfacial water film development and complex multi-cation carbonate precipitates.

Using the Avrami equation, which is used to describe solid transformations between phases at a constant temperature,^{17, 70} the rate constants were derived for each temperature (Table 1). Increases in reaction extent with time are described by the Avrami mode, and herein we have no evidence for reaction inhibition via surface passivation. The linear slope of the Avrami rate constants indicates that the carbonation is proceeding through the same mechanism between temperatures, and the different time-dependent phase assemblages (Figure 6A) at our three temperatures are not affecting the observed end product. The Arrhenius plot was then used to fit the rate constants and calculate the activation energy of diopside carbonation to be 97 ± 16 kJ/mol (Figure 6C). This value aligns with the activation energy of diopside dissolution, 96.1 kJ/mol,¹¹² which implies the

dissolution of diopside is the rate-determining step in the carbonation reaction.

Molecular insights into the surface stability of diopside

Our DFT calculations for the diopside surface provided insight into the dissolution susceptibility of a mixed-cation inosilicate. The (110) surface cleavage is considered here as it is experimentally the most stable surface.¹¹⁶ The (110) surface can be cut at four locations on the z-axis to keep the dipole moment zero (Figure 7). The surface stability indices are calculated for all cases, as shown in Table S1. Case (II) represents the most stable surface, followed by case (III). The surface silicon atoms in cases (I) and (IV) are coordinated with three oxygen atoms and are thus undercoordinated. Conversely, the surface silicon atoms in cases (II) and (III) are coordinated with four oxygen atoms. The silicate chains have an infinite length similar to the silicate chains in the inner bulk layers.

After the surfaces in cases (II) and (III) are relaxed, the distance between the outermost metal ions and the second metal ion layers decreases due to undercoordination. The oxygen coordination numbers for surface metal ions, before and after surface relaxation are shown in Table S2. For case (III), relaxation occurs such that both Ca and Mg surface ions are fully coordinated compared to their bulk coordination numbers. However, for case (II), surface calcium atoms, furthest from the inner layers compared to magnesium atoms, remain undercoordinated with the coordination number of 6. The undercoordination of surface calcium ions could be compensated through bonding with water molecules, ligands, and hydroxyl groups. Such surface complexations can lead to proton- or ligand-promoted dissolution.¹¹⁷⁻¹²²

Environmental implications

Pyroxene is one of the most prevalent mineral groups found in basalt and similar reactive rocks, and is one of the most abundant mafic minerals in the Earth's crust.³⁴ Of these, diopside is commonly found in nature but minimal work has been done to understand the carbonation pathways once injected with CO₂. Our work has verified that the multi-ion composition of diopside means there are a range of carbonate products possible, including transient and amorphous phases. It is important to collect and interpret such time and temperature data for diopside carbonation if it is to be a practical carbon storage solution. The diopside carbonation rates for 50-110°C and the resulting activation energy may be used in conjunction with similar data for other minerals to directly parameterize reactive transport models for CO₂ injection into mafic and ultramafic reservoirs, helping address multi-scale knowledge gaps in complex field environments. When combined with ongoing studies with other mafic minerals, these findings could ultimately help enable implementation of CO₂ injection projects, such as in obtaining permits, developing measuring, reporting, and verifying (MRV) protocols, optimizing injection strategies, and enhancing permanence.

Conclusions

A combination of *in situ* and *ex situ* experiments was used to elucidate the pathways and kinetics of diopside carbonation. XRD, TGA-MS, SEM-EDS, and mass-balance analyses showed that once diopside is exposed to hydrated scCO₂ it rapidly reacts to form a variety of carbonate products, including transient and amorphous phases. Since diopside has two metal cations and carbonation is a continuous dissolution-precipitation process, it is rational that multiple carbonates would result at different times and temperatures. Avrami-derived rate constants for each temperature were plotted and fit the Arrhenius equation to give an activation energy of 97 ± 16 kJ/mol, similar to the energy of diopside dissolution. Computational studies provided molecular insight into the surface stabilities of the different faces of diopside, indicating that the undercoordinated calcium atoms at the diopside/vacuum interface are prone to dissolution when in contact with water. Our results provide valuable insight into the mechanisms of diopside carbonation and its role in the fate and transport of CO₂ injected into basalt and other mafic-ultramafic rocks for permanent storage. These types of fundamental measurements and complementary molecular simulations are poised to help enable CCS and CDR technologies and achieve carbon-negative goals worldwide.

Conflicts of Interest

There are no conflicts to declare.

Author ORCID Information

BA: 0000-0001-5997-3737
LH: 0000-0001-5730-3182
HTS: 0000-0002-4546-3979
SV: 0000-0002-2073-3442

MJAQ: 0000-0001-6911-0994
JVC: 0000-0001-9197-0878
JEH: 0000-0002-9094-8553
ETR: 0000-0003-2152-0067
LMA: 0000-0002-2609-8750
KMR: 0000-0002-8474-7720
QRSM: 0000-0003-3009-9702

Acknowledgements

This material is based on work supported by the U.S. Department of Energy (DOE), Office of Science, Office of Basic Energy Sciences (BES), Chemical Sciences, Geosciences, and Biosciences Division through its Geosciences program at Pacific Northwest National Laboratory (PNNL), FWP 56674. BA and LH were supported by the DOE, Office of Science, Office of Workforce Development for Teachers and Scientists (WDTS) under the Visiting Faculty Program (VFP). JEH and HTS were supported by Darin Damiani (DOE HQ) and the DOE Office of Fossil Energy at PNNL through the National Energy Technology Laboratory, Morgantown, West Virginia. HTS also acknowledges support from the Carbon Utilization and Storage Partnership (CUSP). SV and MJAQ were supported by the DOE Office of Science BES through an Early Career Award to MJAQ (DE-SC0022301). Work by LMA was supported by the U.S. Department of Energy, Office of Science, Office of Basic Energy Sciences, Chemical Sciences, Geosciences, and Biosciences Division. We thank Michael C. Perkins (PNNL) for graphics support. Lastly, we would like to thank the three anonymous reviewers for their time and attention, which helped improve the manuscript.

Notice of copyright: This manuscript has been co-authored by UT-Battelle, LLC, under contract DE-AC05-00OR22725 with the DOE. The publisher acknowledges the US government license to provide public access under the DOE Public Access Plan (<http://energy.gov/downloads/doe-public-access-plan>).

References

1. IEA, *Global Energy Review: CO₂ Emissions in 2021*, IEA, Paris, 2022.
2. S. Krevor, H. de Coninck, S. E. Gasda, N. S. Ghaleigh, V. de Gooyert, H. Hajibeygi, R. Juanes, J. Neufeld, J. J. Roberts and F. Swennenhuis, Subsurface carbon dioxide and hydrogen storage for a sustainable energy future, *Nature Reviews Earth & Environment*, 2023, DOI: 10.1038/s43017-022-00376-8.
3. S. R. Gislason and E. H. Oelkers, Carbon Storage in Basalt, *Science*, 2014, **344**, 373-374.
4. B. P. McGrail, H. T. Schaefer, A. M. Ho, Y.-J. Chien, J. J. Dooley and C. L. Davidson, Potential for carbon dioxide sequestration in flood basalts, *J. Geophys. Res. Solid Earth*, 2006, **111**.
5. J. M. Matter and P. B. Kelemen, Permanent storage of carbon dioxide in geological reservoirs by mineral carbonation, *Nat. Geosci.*, 2009, **2**, 837-841.

- 1
2
3
4
5
6
7
8
9
10
11
12
13
14
15
16
17
18
19
20
21
22
23
24
25
26
27
28
29
30
31
32
33
34
35
36
37
38
39
40
41
42
43
44
45
46
47
48
49
50
51
52
53
54
55
56
57
58
59
60
6. S. Bachu, W. D. Gunter and E. H. Perkins, Aquifer disposal of CO₂-hydrodynamic and mineral trapping, *Energy Convers. Manage.*, 1994, **35**, 269-274.
7. K. Madhu, S. Pauliuk, S. Dhathri and F. Creutzig, Understanding environmental trade-offs and resource demand of direct air capture technologies through comparative life-cycle assessment, *Nature Energy*, 2021, DOI: 10.1038/s41560-021-00922-6.
8. S. K. White, F. A. Spane, H. T. Schaeff, Q. R. S. Miller, M. D. White, J. A. Horner and B. P. McGrail, Quantification of CO₂ Mineralization at the Wallula Basalt Pilot Project, *Environ. Sci. Technol.*, 2020, **54**, 14609-14616.
9. B. P. McGrail, H. T. Schaeff, F. A. Spane, J. B. Cliff, O. Qafoku, J. A. Horner, C. J. Thompson, A. T. Owen and C. E. Sullivan, Field Validation of Supercritical CO₂ Reactivity with Basalts, *Environ. Sci. & Technol. Lett.*, 2017, **4**, 6-10.
10. J. M. Matter, M. Stute, S. O. Snaebjornsdottir, E. H. Oelkers, S. R. Gislason, E. S. Aradottir, B. Sigfusson, I. Gunnarsson, H. Sigurdardottir, E. Gunnlaugsson, G. Axelsson, H. A. Alfredsson, D. Wolff-Boenisch, K. Mesfin, D. F. D. Taya, J. Hall, K. Dideriksen and W. S. Broecker, Rapid carbon mineralization for permanent disposal of anthropogenic carbon dioxide emissions, *Science*, 2016, **352**, 1312-1314.
11. E. G. Polites, H. T. Schaeff, J. A. Horner, A. T. Owen, J. E. Holliman Jr, B. P. McGrail and Q. R. S. Miller, Exotic Carbonate Mineralization Recovered from a Deep Basalt Carbon Storage Demonstration, *Environ. Sci. Technol.*, 2022, **56**, 14713-14722.
12. C. T. Depp, Q. R. S. Miller, J. V. Crum, J. A. Horner and H. T. Schaeff, Pore-Scale Microenvironments Control Anthropogenic Carbon Mineralization Outcomes in Basalt, *ACS Earth and Space Chemistry*, 2022, **6**, 2836-2847.
13. P. A. E. Pogge von Strandmann, K. W. Burton, S. O. Snaebjornsdottir, B. Sigfusson, E. S. Aradottir, I. Gunnarsson, H. A. Alfredsson, K. G. Mesfin, E. H. Oelkers and S. R. Gislason, Rapid CO₂ mineralisation into calcite at the CarbFix storage site quantified using calcium isotopes, *Nat. Comm.*, 2019, **10**, 1983.
14. M. J. A. Qomi, Q. R. S. Miller, S. Zare, H. T. Schaeff, J. P. Kaszuba and K. M. Rosso, Molecular-Scale Mechanisms of CO₂ Mineralization in Nanoscale Interfacial Water Films, *Nature Reviews Chemistry* 2022, **6**, 598-613.
15. S. Ó. Snaebjornsdottir, B. Sigfusson, C. Marieni, D. Goldberg, S. R. Gislason and E. H. Oelkers, Carbon dioxide storage through mineral carbonation, *Nature Reviews Earth & Environment*, 2020, **1**, 90-102.
16. E. H. Oelkers, J. Declercq, G. D. Saldi, S. R. Gislason and J. Schott, Olivine dissolution rates: A critical review, *Chemical Geology*, 2018, **500**, 1-19.
17. Q. R. S. Miller, H. T. Schaeff, J. P. Kaszuba, G. Gadikota, B. P. McGrail and K. M. Rosso, Quantitative Review of Olivine Carbonation Kinetics: Reactivity Trends, Mechanistic Insights, and Research Frontiers, *Environ. Sci. & Technol. Lett.*, 2019, **6**, 431-442.
18. E. Sendula, H. M. Lamadrid, J. D. Rimstidt, M. Steele-MacInnis, D. M. Sublett, L. E. Aradi, C. Szabó, M. J. Caddick, Z. Zajacz and R. J. Bodnar, Synthetic Fluid Inclusions XXIV. In situ Monitoring of the Carbonation of Olivine Under Conditions Relevant to Carbon Capture and Storage Using Synthetic Fluid Inclusion Micro-Reactors: Determination of Reaction Rates, *Frontiers in Climate*, 2021, **3**.
19. J. S. Loring, Q. R. S. Miller, C. J. Thompson and H. T. Schaeff, in *Science of Carbon Storage in Deep Saline Formations*, Elsevier, 2019, pp. 47-65.
20. S. Zare, K. M. S. Uddin, A. Funk, Q. R. S. Miller and M. J. A. Qomi, Nanoconfinement matters in humidified CO₂ interaction with metal silicates, *Environmental Science: Nano*, 2022, **9**, 3766-3779.
21. Q. R. S. Miller, J. P. Kaszuba, S. N. Kerisit, H. T. Schaeff, M. E. Bowden, B. P. McGrail and K. M. Rosso, Emerging investigator series: ion diffusivities in nanoconfined interfacial water films contribute to mineral carbonation thresholds, *Environmental Science: Nano*, 2020, **7**, 1068-1081.
22. Q. R. S. Miller and H. T. Schaeff, Activation energy of magnesite (MgCO₃) precipitation: recent insights from olivine carbonation studies, *Environmental Science: Advances*, 2022.
23. J. S. Loring, C. J. Thompson, Z. Wang, A. G. Joly, D. S. Sklarew, H. T. Schaeff, E. S. Ilton, K. M. Rosso and A. R. Felmy, In Situ Infrared Spectroscopic Study of Forsterite Carbonation in Wet Supercritical CO₂, *Environ. Sci. Technol.*, 2011, **45**, 6204-6210.
24. J. S. Loring, J. Chen, P. Benezeth, O. Qafoku, E. S. Ilton, N. M. Washton, C. J. Thompson, P. F. Martin, B. P. McGrail, K. M. Rosso, A. R. Felmy and H. T. Schaeff, Evidence for carbonate surface complexation during forsterite carbonation in wet supercritical carbon dioxide, *Langmuir*, 2015, **31**, 7533-7543.
25. H. T. Schaeff, B. P. McGrail, J. L. Loring, M. E. Bowden, B. W. Arey and K. M. Rosso, Forsterite [Mg₂SiO₄] Carbonation in Wet Supercritical CO₂: An in Situ High-Pressure X-ray Diffraction Study, *Environ. Sci. Technol.*, 2013, **47**, 174-181.
26. H. T. Schaeff, Q. R. S. Miller, C. J. Thompson, J. S. Loring, M. S. Bowden, B. W. Arey, B. P. McGrail and K. M. Rosso, Silicate carbonation in supercritical CO₂ containing dissolved H₂O: An in situ high pressure X-ray diffraction and infrared spectroscopy study, *Energy Procedia*, 2013, **37**, 5892-5896.
27. D. Zhou, S. Cao, J. Liu, X. Li, Y. Dong, F. Neubauer, J. Bai and H. Li, Carbonation and serpentinization of diopside in the Altun Mountains, NW China, *Scientific Reports*, 2022, **12**, 21361.
28. F. Piccoli, A. Vitale Brovarone and J. J. Ague, Field and petrological study of metasomatism and high-pressure carbonation from lawsonite eclogite-facies terrains, Alpine Corsica, *Lithos*, 2018, **304-307**, 16-37.
29. A. Bouissonnié, D. Daval and P. Ackerer, Dissolution Anisotropy of Pyroxenes: A Surrogate Model for Steady-State Enstatite Dissolution Resulting from Stochastic Simulations of the Hydrolysis Process, *J. Phys. Chem. C*, 2020, **124**, 13113-13126.
30. A. Bouissonnié, D. Daval and P. Ackerer, Dissolution Anisotropy of Pyroxenes: Role of Edges and Corners Inferred from Stochastic Simulations of Enstatite Dissolution, *J. Phys. Chem. C*, 2021, **125**, 7658-7674.
31. A. Bouissonnié, D. Daval, F. Guyot and P. Ackerer, The Dissolution Anisotropy of Pyroxenes: Experimental Validation of a Stochastic Dissolution Model Based on Enstatite Dissolution, *J. Phys. Chem. C*, 2020, **124**, 3122-3140.
32. D. Daval, R. Hellmann, G. D. Saldi, R. Wirth and K. G. Knauss, Linking nm-scale measurements of the anisotropy of

- silicate surface reactivity to macroscopic dissolution rate laws: New insights based on diopside, *Geochimica et Cosmochimica Acta*, 2013, **107**, 121-134.
33. C. M. Phillips-Lander, A. S. Elwood Madden, E. M. Hausrath and M. E. Elwood Madden, Aqueous alteration of pyroxene in sulfate, chloride, and perchlorate brines: Implications for post-Noachian aqueous alteration on Mars, *Geochimica et Cosmochimica Acta*, 2019, **257**, 336-353.
34. K. G. Knauss, S. N. Nguyen and H. C. Weed, Diopside dissolution kinetics as a function of pH, CO₂, temperature, and time, *Geochimica et Cosmochimica Acta*, 1993, **57**, 285-294.
35. D. I. Siegel and H. O. Pfannkuch, Silicate mineral dissolution at pH 4 and near standard temperature and pressure, *Geochimica et Cosmochimica Acta*, 1984, **48**, 197-201.
36. J. Schott and R. A. Berner, in *The chemistry of weathering*, Springer, 1985, pp. 35-53.
37. J.-C. Petit, G. D. Mea, J.-C. Dran, J. Schott and R. A. Berner, Mechanism of diopside dissolution from hydrogen depth profiling, *Nature*, 1987, **325**, 705-707.
38. J. Schott, R. A. Berner and E. L. Sjöberg, Mechanism of pyroxene and amphibole weathering—I. Experimental studies of iron-free minerals, *Geochimica et Cosmochimica Acta*, 1981, **45**, 2123-2135.
39. E. H. Oelkers, in *Growth, Dissolution and Pattern Formation in Geosystems*, eds. B. Jamtveit and P. Meakin, Springer Netherlands, 1999, ch. 12, pp. 253-267
40. E. H. Oelkers and J. Schott, An experimental study of enstatite dissolution rates as a function of pH, temperature, and aqueous Mg and Si concentration, and the mechanism of pyroxene/pyroxenoid dissolution, *Geochimica et Cosmochimica Acta*, 2001, **65**, 1219-1231.
41. H. U. Sverdrup, *The kinetics of base cation release due to chemical weathering*, Krieger Publishing Company, 1990.
42. S. Dixit and S. A. Carroll, Effect of solution saturation state and temperature on diopside dissolution, *Geochem. Trans.*, 2007, **8**, 1-14.
43. Y. Chen and S. L. Brantley, Diopside and anthophyllite dissolution at 25° and 90°C and acid pH, *Chemical Geology*, 1998, **147**, 233-248.
44. S. L. Brantley and Y. Chen, in *Chemical weathering rates of silicate minerals*, eds. A. F. White and S. L. Brantley, Mineralogical Society of America, Washington D.C., 1995, vol. 31, pp. 119-172.
45. L. Monasterio-Guillot, C. Rodriguez-Navarro and E. Ruiz-Agudo, Kinetics and Mechanisms of Acid-pH Weathering of Pyroxenes, *GGG*, 2021, **22**, e2021GC009711.
46. M. Heřmanská, M. J. Voigt, C. Marieni, J. Declercq and E. H. Oelkers, A comprehensive and internally consistent mineral dissolution rate database: Part I: Primary silicate minerals and glasses, *Chem. Geol.*, 2022, **597**, 120807.
47. G. Stockmann, D. Wolff-Boenisch, S. R. Gislason and E. H. Oelkers, Dissolution of diopside and basaltic glass: the effect of carbonate coating, *Mineralogical Magazine*, 2008, **72**, 135-139.
48. D. Daval, R. Hellmann, J. Corvisier, D. Tisserand, I. Martinez and F. Guyot, Dissolution kinetics of diopside as a function of solution saturation state: Macroscopic measurements and implications for modeling of geological storage of CO₂, *Geochimica et Cosmochimica Acta*, 2010, **74**, 2615-2633.
49. G. J. Stockmann, D. Wolff-Boenisch, S. R. Gislason and E. H. Oelkers, Do carbonate precipitates affect dissolution kinetics?: 2: Diopside, *Chemical Geology*, 2013, **337-338**, 56-66.
50. M. Bodor, R. M. Santos, L. Kriskova, J. Elsen, M. Vlad and T. Van Gerven, Susceptibility of mineral phases of steel slags towards carbonation: mineralogical, morphological and chemical assessment, *Eur. J. Mineral.*, 2013, **25**, 533-549.
51. Y. E. Chai, Q. R. S. Miller, H. T. Schaeff, D. Barpaga, R. Bakhshoodeh, M. Bodor, T. Van Gerven and R. M. Santos, Pressurized in situ X-ray diffraction insights into super/subcritical carbonation reaction pathways of steelmaking slags and constituent silicate minerals, *The Journal of Supercritical Fluids*, 2021, **171**, 105191.
52. J. S. Loring, Q. R. S. Miller, H. T. Schaeff and C. J. Thompson, in *Science of Carbon Storage in Deep Saline Formations: Process Coupling across Time and Spatial Scales*, eds. P. Newell and A. G. Ilgen, Elsevier, 1st edn., 2018.
53. L. Monasterio-Guillot, F. Di Lorenzo, E. Ruiz-Agudo and C. Rodriguez-Navarro, Reaction of pseudowollastonite with carbonate-bearing fluids: Implications for CO₂ mineral sequestration, *Chemical Geology*, 2019, **524**, 158-173.
54. L. Monasterio-Guillot, A. Fernandez-Martinez, E. Ruiz-Agudo and C. Rodriguez-Navarro, Carbonation of calcium-magnesium pyroxenes: Physical-chemical controls and effects of reaction-driven fracturing, *Geochimica et Cosmochimica Acta*, 2021, **304**, 258-280.
55. F. Wang, D. Dreisinger, M. Jarvis and T. Hitchins, Kinetic evaluation of mineral carbonation of natural silicate samples, *Chemical Engineering Journal*, 2021, **404**, 126522.
56. G. Gadikota, J. Matter, P. Kelemen, P. V. Brady and A.-H. A. Park, Elucidating the differences in the carbon mineralization behaviors of calcium and magnesium bearing alumino-silicates and magnesium silicates for CO₂ storage, *Fuel*, 2020, **277**, 117900.
57. D. Jiang, S. Dong, L. Zhao and H. Teng, San Francisco, CA, 2013.
58. A. M. Kalinkin, A. A. Politov, V. V. Boldyrev, E. V. Kalinkina, V. N. Makarov and V. T. Kalinnikov, Mechanical Activation of Diopside in CO₂, *Inorganic Materials*, 2002, **38**, 163-167.
59. R. J. Bodnar, M. Steele-MacInnis, R. M. Capobianco, J. D. Rimstidt, R. Dilmore, A. Goodman and G. Guthrie, PVTX Properties of H₂O-CO₂-"salt" at PTX Conditions Applicable to Carbon Sequestration in Saline Formations, *Geochemistry of Geologic CO₂ Sequestration*, 2013, **77**, 123-152.
60. E. Tajuelo Rodriguez, L. M. Anovitz, C. D. Clement, A. J. Rondinone and M. C. Cheshire, Facile emulsion mediated synthesis of phase-pure diopside nanoparticles, *Sci. Rep.*, 2018, **8**, 3099.
61. H. T. Schaeff, B. P. McGrail, J. L. Loring, M. E. Bowden, B. W. Arey and K. M. Rosso, Forsterite [Mg₂SiO₄] carbonation in wet supercritical CO₂: An in situ high pressure X-ray diffraction study, *Environ. Sci. Technol.*, 2013, **47**, 174-181.
62. H. T. Schaeff, C. F. Windisch, Jr., B. P. McGrail, P. F. Martin and K. M. Rosso, Brucite Mg(OH)₂ carbonation in wet supercritical CO₂: An in situ high pressure X-ray diffraction study, *Geochimica et Cosmochimica Acta*, 2011, **75**, 7458-7471.
63. Q. R. S. Miller, C. J. Thompson, J. S. Loring, C. F. Windisch, M. E. Bowden, D. W. Hoyt, J. Z. Hu, B. W. Arey, K. M. Rosso and H. T. Schaeff, Insights into silicate carbonation processes in water-bearing supercritical CO₂ fluids, *Int. J. Greenhouse Gas Control*, 2013, **15**, 104-118.

64. Q. R. S. Miller, J. P. Kaszuba, H. T. Schaef, M. E. Bowden and B. P. McGrail, Impacts of organic ligands on forsterite reactivity in supercritical CO₂ fluids, *Environ. Sci. Technol.*, 2015, **49**, 4724-4734.
65. Q. R. S. Miller, H. T. Schaef, J. P. Kaszuba, L. Qiu, M. E. Bowden and B. P. McGrail, Tunable Manipulation of Mineral Carbonation Kinetics in Nanoscale Water Films via Citrate Additives, *Environmental Science & Technology*, 2018, **52**, 7138-7148.
66. R. Span and W. Wagner, A new equation of state for carbon dioxide covering the fluid region from the triple-point temperature to 1100 K at pressures up to 800 MPa, *Journal of Physical and Chemical Reference Data*, 1996, **25**, 1509-1596.
67. R. D. Springer, Z. Wang, A. Anderko, P. Wang and A. R. Felmy, A thermodynamic model for predicting mineral reactivity in supercritical carbon dioxide: I. Phase behavior of carbon dioxide-water-chloride salt systems across the H₂O-rich to the CO₂-rich regions, *Chemical Geology*, 2012, **322**, 151-171.
68. Q. R. S. Miller, D. A. Dixon, S. D. Burton, E. D. Walter, D. W. Hoyt, A. S. McNeill, J. D. Moon, K. S. Thanthirawatte, E. S. Ilton, O. Qafoku, C. J. Thompson, H. T. Schaef, K. M. Rosso and J. S. Loring, Surface-catalyzed oxygen exchange during carbonation in nanoscale water films, *J. Phys. Chem. C*, 2019, **120**, 12871-12885.
69. Q. R. S. Miller, J. P. Kaszuba, H. T. Schaef, M. E. Bowden, B. P. McGrail and K. M. Rosso, Anomalous low activation energy of nanoconfined MgCO₃ precipitation, *Chemical Communications*, 2019, **55**, 6835-6837.
70. M. A. Sinnwell, Q. R. S. Miller, L. Liu, J. Tao, M. E. Bowden, L. Kovarik, D. Barpaga, Y. Han, R. Kishan Motkuri, M. L. Sushko, H. T. Schaef and P. K. Thallapally, Kinetics and Mechanisms of ZnO to ZIF-8 Transformations in Supercritical CO₂ Revealed by In Situ X-ray Diffraction, *ChemSusChem*, 2020, **13**, 2602-2612.
71. M. Avrami, Kinetics of Phase Change. II Transformation-Time Relations for Random Distribution of Nuclei, *J. Chem. Phys.*, 1940, **8**, 212-224.
72. J. P. Perrillat, Kinetics of high-pressure mineral phase transformations using in situ time-resolved X-ray diffraction in the Paris-Edinburgh cell: A practical guide for data acquisition and treatment, *Mineralogical Magazine*, 2008, **72**, 683-695.
73. A. Cattaneo, A. Gualtieri and G. Artioli, Kinetic study of the dehydroxylation of chrysotile asbestos with temperature by in situ XRPD, *Physics and Chemistry of Minerals*, 2003, **30**, 177-183.
74. J. P. Perrillat, I. Daniel, K. T. Koga, B. Reynard, H. Cardon and W. A. Crichton, Kinetics of antigorite dehydration: A real-time X-ray diffraction study, *Earth and Planetary Science Letters*, 2005, **236**, 899-913.
75. J. D. Hancock and J. H. Sharp, Method of comparing solid-state kinetic data and its application to the decomposition of kaolinite, brucite, and BaCO₃, *J. Am. Ceram. Soc.*, 1972, **55**, 74-77.
76. J. P. Perrillat, I. Daniel, J.-M. Lardeaux and H. Cardon, Kinetics of the coesite-quartz transition: Application to the exhumation of ultrahigh-pressure rocks, *Journal of Petrology*, 2003, **44**, 773-788.
77. J. D. Rimstidt, *Geochemical Rate Models: An Introduction to Geochemical Kinetics*, Cambridge University Press, 2013.
78. M. J. Van Vleet, T. Weng, X. Li and J. R. Schmidt, In Situ, Time-Resolved, and Mechanistic Studies of Metal–Organic Framework Nucleation and Growth, *Chem. Rev.*, 2018, **118**, 3681-3721.
79. V. Nikulshina, M. E. Gálvez and A. Steinfeld, Kinetic analysis of the carbonation reactions for the capture of CO₂ from air via the Ca(OH)₂–CaCO₃–CaO solar thermochemical cycle, *Chem. Eng. J.*, 2007, **129**, 75-83.
80. A. Aftree-Williams, A. Pring, Y. Ngothai and J. Brugger, The Carbonation of Anhydrite: Kinetics and Reaction Pathways, *ACS Earth and Space Chemistry*, 2017, **1**, 89-100.
81. G. Kresse and J. Furthmüller, Efficient iterative schemes for ab initio total-energy calculations using a plane-wave basis set, *Physical review B*, 1996, **54**, 11169.
82. G. Kresse and D. Joubert, From ultrasoft pseudopotentials to the projector augmented-wave method, *Physical review b*, 1999, **59**, 1758.
83. J. P. Perdew, K. Burke and M. Ernzerhof, Generalized gradient approximation made simple, *Physical Review Letters*, 1996, **77**, 3865-3868.
84. G. Stanger and C. Neal, The occurrence and chemistry of huntite from Oman, *Chem. Geol.*, 1994, **112**, 247-254.
85. D. J. J. Kinsman, Huntite from a carbonate-evaporite environment, *American Mineralogist: Journal of Earth and Planetary Materials*, 1967, **52**, 1332-1340.
86. D. L. Graf and W. F. Bradley, The crystal structure of huntite, Mg₃Ca(CO₃)₄, *Acta Crystallogr.*, 1962, **15**, 238-242.
87. G. T. Faust, Huntite, Mg₃Ca(CO₃)₄ A new mineral, *American Mineralogist: Journal of Earth and Planetary Materials*, 1953, **38**, 4-24.
88. W. A. Dollase and R. J. Reeder, Crystal structure refinement of huntite, CaMg₃(CO₃)₄, with X-ray powder data, *Am. Mineral.*, 1986, **71**, 163-166.
89. F. Lippmann, *Sedimentary Carbonate Minerals*, Springer Berlin Heidelberg, Berlin, Heidelberg, 1973.
90. I. J. Kell-Duivesteyn, A. Baldermann, V. Mavromatis and M. Dietzel, Controls of temperature, alkalinity and calcium carbonate reactant on the evolution of dolomite and magnesite stoichiometry and dolomite cation ordering degree—An experimental approach, *Chemical Geology*, 2019, **529**, 119292.
91. P. J. Davies, B. Bubela and J. Ferguson, Simulation of carbonate diagenetic processes: formation of dolomite, huntite and monohydrocalcite by the reactions between nesquehonite and brine, *Chemical Geology*, 1977, **19**, 187-214.
92. L. Hopkinson, K. Rutt and G. Cressey, The transformation of nesquehonite to hydromagnesite in the system CaO–MgO–H₂O–CO₂: An experimental spectroscopic study, *Journal of Geology*, 2008, **116**, 387-400.
93. M. Sánchez-Román, C. S. Romanek, D. C. Fernández-Remolar, A. Sánchez-Navas, J. A. McKenzie, R. A. Pibernat and C. Vasconcelos, Aerobic biomineralization of Mg-rich carbonates: Implications for natural environments, *Chemical Geology*, 2011, **281**, 143-150.
94. V. Vandeginste, Effect of pH Cycling and Zinc Ions on Calcium and Magnesium Carbonate Formation in Saline Fluids at Low Temperature, *Minerals*, 2021, **11**, 723.
95. R. A. Berner, The role of magnesium in the crystal growth of calcite and aragonite from sea water, *Geochim. Cosmochim. Acta*, 1975, **39**, 489-504.

Journal Name

ARTICLE

96. K. J. Davis, P. M. Dove and J. J. De Yoreo, The role of Mg²⁺ as an impurity in calcite growth, *Science*, 2000, **290**, 1134-1137.
97. M. M. Reddy and K. K. Wang, Crystallization of calcium carbonate in the presence of metal ions: I. Inhibition by magnesium ion at pH 8.8 and 25 C, *J. Cryst. Growth*, 1980, **50**, 470-480.
98. L. A. Hollingbery and T. R. Hull, The thermal decomposition of huntite and hydromagnesite—a review, *Thermochim. Acta*, 2010, **509**, 1-11.
99. M. Földvári, *Handbook of thermogravimetric system of minerals and its use in geological practice*, Geological Institute of Hungary Budapest, 2011.
100. Y. Fang and H. Xu, A New Approach To Quantify the Ordering State of Protodolomite Using XRD, TEM, and Z-Contrast Imaging, *J. Sediment. Res.*, 2019, **89**, 537-551.
101. J. M. Gregg, D. L. Bish, S. E. Kaczmarek and H. G. Machel, Mineralogy, nucleation and growth of dolomite in the laboratory and sedimentary environment: a review, *Sedimentology*, 2015, **62**, 1749-1769.
102. N. Floquet, D. Vielzeuf, V. Heresanu, D. Laporte and J. Perrin, Synchrotron high-resolution XRD and thermal expansion of synthetic Mg calcites, *Physics and Chemistry of Minerals*, 2020, **47**, 1-20.
103. D. L. Graf and J. R. Goldsmith, Some hydrothermal syntheses of dolomite and protodolomite, *The Journal of Geology*, 1956, **64**, 173-186.
104. J. C. Deelman, Low-temperature nucleation of magnesite and dolomite, *Neu. Jb. Mineral Mh.*, 1999, 289-302.
105. S. T. Mergelsberg, J. J. De Yoreo, Q. R. S. Miller, F. Marc Michel, R. N. Ulrich and P. M. Dove, Metastable solubility and local structure of amorphous calcium carbonate (ACC), *Geochimica et Cosmochimica Acta*, 2020, **289**, 196-206.
106. G.-i. Yamamoto, A. Kyono and S. Okada, Temperature dependence of amorphous magnesium carbonate structure studied by PDF and XAFS analyses, *Sci. Rep.*, 2021, **11**, 22876.
107. G. Montes-Hernandez, F. Renard, A.-L. Auzende and N. Findling, Amorphous Calcium–Magnesium Carbonate (ACMC) Accelerates Dolomitization at Room Temperature under Abiotic Conditions, *Cryst. Growth Des.*, 2020, **20**, 1434-1441.
108. B. Purgstaller, K. E. Goetschl, V. Mavromatis and M. Dietzel, Solubility investigations in the amorphous calcium magnesium carbonate system, *CrystEngComm*, 2019, **21**, 155-164.
109. D. N. Lumsden, Discrepancy between thin-section and X-ray estimates of dolomite in limestone, *Journal of Sedimentary Research*, 1979, **49**, 429-435.
110. B. Purgstaller, V. Mavromatis, K. E. Goetschl, F. R. Steindl and M. Dietzel, Effect of temperature on the transformation of amorphous calcium magnesium carbonate with near-dolomite stoichiometry into high Mg-calcite, *CrystEngComm*, 2021, **23**, 1969-1981.
111. C. M. Pina, C. Pimentel and A. n. Crespo, The Dolomite Problem: A Matter of Time, *ACS Earth and Space Chemistry*, 2022.
112. J. L. Palandri and Y. K. Kharaka, *A compilation of rate parameters of water-mineral interaction kinetics for application to geochemical modeling*, Report Open File Report 2004-1068, United States Geological Survey, Menlo Park, California, 2004.
113. H. Schaef, C. Thompson, J. Loring, M. Bowden, B. Arey, B. McGrail and K. Rosso, Silicate carbonation in supercritical CO₂ containing dissolved H₂O: An in situ high pressure X-ray diffraction and infrared spectroscopy study, *Energy Procedia*, 2013, **37**, 5892-5896.
114. C. M. Bethke, *Geochemical and Biogeochemical Reaction Modeling*, 2008.
115. J. P. Kaszuba, H. S. Viswanathan and J. W. Carey, Relative stability and significance of dawsonite and aluminum minerals in geologic carbon sequestration, *Geophysical Research Letters*, 2011, **38**.
116. J. W. Anthony, R. A. Bideaux, K. W. Bladh and M. C. Nichols, *Handbook of Mineralogy*, Mineral Data Publ., Tuscon, AZ, 2003.
117. R. A. Wogelius and J. V. Walther, Olivine dissolution kinetics at near-surface conditions, *Chemical Geology*, 1992, **97**, 101-112.
118. E. H. Oelkers, S. V. Golubev, C. Chairat, O. S. Pokrovsky and J. Schott, The surface chemistry of multi-oxide silicates, *Geochimica et Cosmochimica Acta*, 2009, **73**, 4617-4634.
119. W. H. Casey, H. R. Westrich, J. F. Banfield, G. Ferruzzi and G. W. Arnold, Leaching and reconstruction at the surface of dissolving chain-silicate minerals, *Nature*, 1993, **366**, 253-256.
120. R. C. Longo, K. Cho, P. Bruner, A. Welle, A. Gerdes and P. Thissen, Carbonation of Wollastonite(001) Competing Hydration: Microscopic Insights from Ion Spectroscopy and Density Functional Theory, *ACS Appl. Mater. Interfaces*, 2015, **7**, 4706-4712.
121. S. Zare, A. Funk and M. J. Abdolhosseini Qomi, Formation and Dissolution of Surface Metal Carbonate Complexes: Implications for Interfacial Carbon Mineralization in Metal Silicates, *J. Phys. Chem. C*, 2022, **126**, 11574-11584.
122. S. Zare and M. J. A. Qomi, Reactive force fields for aqueous and interfacial magnesium carbonate formation, *Physical Chemistry Chemical Physics*, 2021, **23**, 23106-23123.